

# Influences of Larger-Scale Vortex Variability on Tornado Pressure Minima in an Outer-Flow Region: Explorations Using a Parametric Tangential Wind Model

VINCENT T. WOOD

*NOAA/OAR/National Severe Storms Laboratory, Norman, Oklahoma*

ROBIN L. TANAMACHI

*Department of Earth, Atmospheric, and Planetary Sciences, Purdue University, West Lafayette, Indiana*

LUTHER W. WHITE<sup>a</sup>

*Department of Mathematics, University of Oklahoma, Norman, Oklahoma*

(Manuscript received 18 May 2016, in final form 29 December 2016)

## ABSTRACT

Previous studies have neglected to distinguish between a central pressure deficit due to a tornado itself and due to a parent mesocyclone in which the tornado is embedded. To obtain improved understanding of the influences of larger-scale vortex variability on smaller-scale tornado pressure deficits, a parametric tangential wind model supplemented with a cyclostrophic speed equation was used to explore the role that the variability plays in influencing radial pressure deficits by deducing radial pressure deficit distributions from radial profiles of hypothetically superpositioned, dual-maxima tangential velocities in the free atmosphere, where a dominant swirling flow was in approximate cyclostrophic balance. The cyclostrophic approximation was partitioned into two separate components, allowing one to scrutinize and determine which of the concentric vortices contributes most significantly to the tornado pressure minima. The model parametrically constructed a smaller-scale, stronger vortex (rapidly swirling flow) that was centered within a larger-scale, weaker vortex (slowly swirling flow) to represent a tornado centered within a supercell, low-level, parent mesocyclone above a tornado boundary layer. The radial pressure deficit fluctuations were varied by changing one of five key velocity-controlling parameters assigned to one vortex to represent a variety of vortex strengths. Based on eight experiments, the larger-scale, weaker (smaller scale, stronger) vortex contributed less (more) to the total pressure deficit than the smaller-scale, stronger (larger scale, weaker) vortex. The stronger vortex centered within the larger-scale, weaker vortex has a larger central pressure minimum than it does in the absence of the larger-scale vortex.

## 1. Introduction

There have been numerous documented cases of quasi-concentric multiple wind field maxima in a variety of vortex configurations observed at finescale (i.e., with horizontal data spacing 100 m or less) with mobile Doppler radars. [Figure 1](#) illustrates an outstanding example of prominent triple-maxima Doppler azimuthal wind and reflectivity fields collected by

the Doppler-on-Wheels (DOW; [Wurman et al. 1997](#)) radar during VORTEX 95 ([Rasmussen et al. 1994](#)). The triple-maxima rotational couplets in the Doppler velocity signatures of vortex circulations of different scales were distinguished by three inbound (negative value toward the radar) and three outbound (positive value away from the radar) Doppler velocity peaks located at different radii from the signature centers. There was evidence of smaller areas of strong rotation (black circle) with spatial scales of a few hundred meters surrounded by the vortex signature of a medium-sized rotational velocity couplet (blue circle), which in turn was embedded in a larger background, convergent velocity couplet (white curves). Mean

---

<sup>a</sup> Emeritus.

---

*Corresponding author e-mail:* Vincent T. Wood, [vincent.wood@noaa.gov](mailto:vincent.wood@noaa.gov)

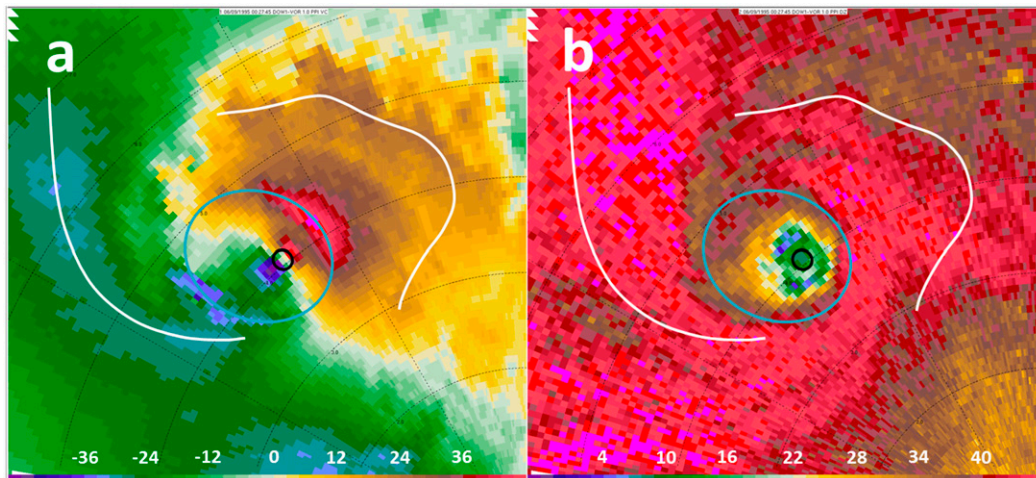


FIG. 1. DOW scans of (a) storm-relative Doppler velocity ( $\text{m s}^{-1}$ ) and (b) reflectivity (dBZ) of the Wheeler, TX, tornado at 0027:45 UTC 9 Jun 1995 during VORTEX 95. (a) Positive (negative) Doppler velocities represent flow away from (toward) the radar. The zero Doppler velocity band represents flow perpendicular to the radar viewing direction. The tornado center (black circle) was located 4.05 km from the radar. At an elevation angle of  $1.0^\circ$ , the beam altitude at this range was 71 m AGL. The black, dashed range rings are marked every 1 km, with dashed spokes provided every  $30^\circ$  in azimuth. The black and blue circles, respectively, represent the approximate vortex sizes of the smaller- and medium-scale vortex circulations. The white curves outside the blue circle denote a possible Doppler velocity couplet of a larger scale but weak vortex circulation pattern. Doppler velocity and reflectivity scales are indicated at the bottom. Storm motion is  $9 \text{ m s}^{-1}$  from  $169^\circ$ . (Radar image courtesy of J. Wurman of the Center for Severe Weather Research.)

rotational velocity maxima of the smaller-, medium-, and larger-scale rotational couplets, respectively, were 49, 41, and  $31 \text{ m s}^{-1}$  (Fig. 2). The estimated diameters of the couplets, respectively, were 185, 1438, and 2316 m (separated by the black, white, and gray arrows) at a constant range of 4 km from the DOW radar.

Many other examples of concentric tangential wind maxima in various vortex circulations were provided in Marquis et al. (2008), Wurman and Kosiba (2013), Wurman et al. (2014), and Wakimoto et al. (2015), among others, which revealed Doppler velocity signatures of vortex circulations of different scales. To the best of the authors' knowledge, there have been no documented cases of more than three concentric tangential wind maxima in vortices on a spatial scale of 10 km or less.

Atmospheric vortices with dual-maximum tangential winds have been revealed in high-resolution numerical simulations of a near-surface tornado-like vortex centered within a larger-scale background vortex aloft (Wicker and Wilhelmson 1993; Lewellen et al. 2000; Lewellen and Lewellen 2007; Davies-Jones 2008; Lewellen 2014). Lewellen et al. (2000) and Lewellen and Lewellen (2007) noted that vortex surface pressure and wind distributions depended on both the structure of the vortex aloft and the detailed structure of the corner flow region. Additionally, they observed that

double-pressure minima responded to the dual-maxima tangential velocities at some low altitudes.

As of this writing, no feasible means exists to obtain pressure measurements within the core flow region of a tornado above the boundary layer (i.e., where the effects of surface friction become vanishingly small). However, many studies have been published in which in situ probes made near-ground pressure and wind measurements within close range of an intercepted tornado (Bluestein 1983; Winn et al. 1999; Markowski et al. 2002; Lee et al. 2004; Samaras and Lee 2004; Wurman and Samaras 2004; Blair et al. 2008; Kato et al. 2015). It is unclear in these cases whether researchers using the probe measurements recognize whether the measurements result from the tornado itself or from the tornado being embedded in the supercell, low-level mesocyclone. Karstens et al. (2010) documented recorded pressure deficits in the pressure time series plots, thereby yielding some clues on how tornado pressure drops varied with time. On the basis of seven of their nine documented cases, the intercepted tornado occurred within the region of the radar-indicated or visually identified mesocyclone. Augmented with videography and eyewitness accounts, Karstens et al. attempted to surmise vortex structure ranging from low-swirl single-celled vortices through medium-swirl two-celled vortices to high

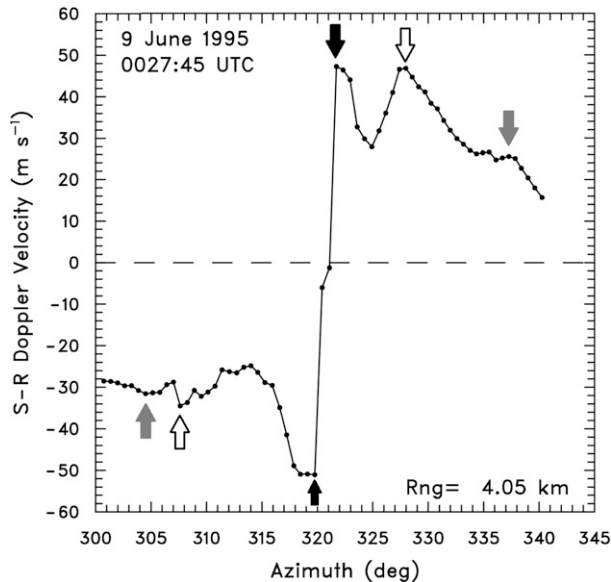


FIG. 2. Azimuthal profile of storm-relative Doppler velocities across the smaller-, medium-, and larger-scale vortex signatures approximately centered at 4 km from the DOW radar at 0027:45 UTC 9 Jun 1995 during VORTEX 95. The dotted curve represents the azimuthal profile of data points. The black and white arrows denote Doppler velocity signatures of smaller- and medium-scale vortex circulations, respectively, as shown in Fig. 1a. The gray arrow indicates the Doppler velocity signatures of a possible larger-scale vortex circulation pattern. At an elevation angle of  $1.0^\circ$ , the beam altitude at this range was 71 m AGL. (Based on Doppler velocity data provided by J. Wurman of the Center for Severe Weather Research.)

swirl-ratio two-celled multiple vortex tornadoes by scrutinizing and interpreting the shape profiles of recorded pressure drops. Nevertheless, it is not possible to untangle the exact contributions of the measurements from the vortices of different scales. It is our belief that the current generation of in situ probes simply lacks the spatiotemporal resolution for researchers to effectively decouple the pressure deficit contribution of the mesocyclone from that of the tornado.

Since the relative contribution of a parent mesocyclone to the low pressure at the center of a tornado is not well understood, a couple of questions are raised:

- How do varying radial profiles of dual-maxima tangential velocities of the mesocyclone and tornado affect the total radial pressure profiles?
- How much does the mesocyclone surrounding the tornado contribute to a central pressure minimum?

The objective of this study is to answer the above questions by investigating and evaluating the significant

perturbation pressure (hereafter, perturbation pressure is referred to as pressure) fluctuations deduced from radial profiles of theoretically superpositioned, dual-maxima tangential velocities. Section 2 presents a brief description of multiple concentric vortex structures. A cyclostrophic wind balance for a single vortex is presented in section 3. Section 4 defines a new cyclostrophic schematization for dual concentric vortices. The cyclostrophic speed equation is partitioned into two separate components of pressure deficit and radial pressure gradient force that correspond to the varying dual-maxima tangential wind profiles in order to quantitatively evaluate the significant fluctuations in central pressure deficits as well as radial pressure gradient forces. In section 5, the parametric tangential wind profile model of Wood and White (2013, hereafter WW13) is used to parametrically construct and superposition two different radial profiles of tangential velocities at a given height level to represent a tornado centered within a supercell, low-level parent mesocyclone above the tornado boundary layer. We restrict our attention to the profiles in the outer-flow region where a main swirling flow is in cyclostrophic balance (Snow 1982; Davies-Jones 1986; Bluestein 2013; Bluestein et al. 2014). In other words, surface friction effects are beyond the scope of this study. A main reason for this restricted focus is the lack of a two-dimensional, parametric model that may be used for studying flow in the tornado boundary layer. Eventually, we hope to develop such a model toward which this study serves as an initial step. Section 6 presents experimental results in which representative pressure deficit and radial pressure gradient force profiles are deduced from a hypothetical superposition of varying, dual-maxima tangential velocity profiles in association with a rapidly and slowly rotating columns of swirling flow. A summary and discussion are presented in section 7.

## 2. Multiple concentric vortex structure

As mentioned in the introduction, the triple concentric vortex structure may be considered to be a triple vortex composed of the first, second, and third individual vortex configurations. The hypothesis of a triple-vortex composite in the tangential velocity profiles enables the description of complex tangential velocity distributions. More precise and comprehensive interpretations are possible if we isolate the *primary* tangential wind profile ( $V_p$ ) from the *secondary* ( $V_s$ ) and *tertiary* ( $V_t$ ) tangential velocity profiles (e.g., Wood et al. 2013). The total tangential wind ( $V_T$ ) profile for axisymmetric flow may be partitioned into the  $V_p$ ,  $V_s$ , and

$V_t$  velocity components defined in a cylindrical coordinate system:

$$V_T(r) = V_p(r) + V_s(r) + V_t(r), \quad (1)$$

where  $r$  is the radius of a circular path. Each tangential velocity profile employs key parameters that define different segments encompassing the velocity profile: maximum tangential velocity, vortex radius at which the maximum occurs, and shape parameters that control different parts of the profile (e.g., broadly versus sharply peaked, changes in the inner and outer profiles), as will be described in section 5. In Eq. (1), the vortices are ordered by the maximum tangential wind, regardless of vortex size. In this study, at least two analytical vortices are used, including two different-sized vortices, each of which had two different maximum tangential velocities assigned to it to represent a variety of vortex strengths. For example, a primary (secondary) vortex represents a stronger (weaker) vortex that is a rapidly (slowly) rotating column of swirling flow.

### 3. Cyclostrophic speed equation for a single vortex

A simple Rankine<sup>1</sup> (1882) vortex model supplemented with the cyclostrophic approximation has been widely used by numerous investigators to provide a diagnostic tool for analyzing and interpreting the observed tangential wind and deduced pressure structures in such convective vortices as dust devils (Sinclair 1973), waterspouts (Leverson et al. 1977), tornadoes (Hoecker 1961 among others), and misocyclones (Inoue et al. 2011). Rennó et al. (1998) and Rennó and Bluestein (2001) used the cyclostrophic speed equation to develop a simple thermodynamical theory for dust devils and waterspouts. Compared to the Rankine vortex, the parametrically constructed non-Rankine<sup>2</sup> vortices have a larger central pressure deficit (Wood and White 2013).

For an axisymmetric vortex in a steady-state, inviscid, and incompressible fluid, tangential velocity sufficiently dominates radial velocity so that there is a cyclostrophic

balance between a radially inward-directed pressure gradient force and a radially outward-directed centrifugal force in the outer-flow region (Snow 1982; Davies-Jones 1986; Bluestein 2013; Bluestein et al. 2014). The cyclostrophic approximation is given by

$$\frac{1}{\rho} \frac{\partial P}{\partial r} = \frac{V_C^2(r)}{r}, \quad (2)$$

where  $V_C(r)$  is the cyclostrophic (tangential) wind speed as a function of radius  $r$  from a circulation center to a circular path,  $P$  is pressure with respect to the motionless base state at radial infinity, and  $\rho$  is air density, which is assumed to be constant. According to Davies-Jones (1986), given an idealized Rankine (1882) velocity distribution, the largest radial pressure gradient force,

$$\frac{1}{\rho} \left( \frac{\partial P}{\partial r} \right)_{\max} = \frac{V_x^2}{R_x}, \quad (3)$$

is located at  $r = R_x$ , where  $R_x$  is the core radius at which the Rankine vortex's tangential velocity peak ( $V_x$ ) occurs.

A pressure deficit  $\Delta P = P(r) - P_E$  is obtained by integrating Eq. (2) radially inward from an environmental pressure  $P_E [= P(r \rightarrow \infty)]$  at which the Rankine tangential wind decreases asymptotically to zero infinitely far from the vortex center. Thus, the minimum pressure deficit found at the vortex center ( $r = 0$ ) is

$$\frac{1}{\rho} (\Delta P)_{\min} = -V_x^2. \quad (4)$$

In Eq. (3) or (4), knowledge of either the maximum Rankine tangential velocity or central pressure deficit above a tornado boundary layer allows the other one to be crudely estimated (e.g., Wakimoto and Wilson 1989; Tanamachi et al. 2013). The utility of Eq. (3) or (4), however, is limited, because the equations are applied to only a single Rankine vortex without being embedded in a larger-scale, background vortex. Equation (2) can be valid for arbitrary radial profiles that can portray either single or multiple wind maxima. A new cyclostrophic schematization for dual concentric vortices may be possible, as will be discussed in detail in the next section.

### 4. New cyclostrophic schematization for dual concentric vortices

We assume that dual concentric, convective vortices are in quasi-steady state and approximately in cyclostrophic balance above the tornado boundary layer so that we

<sup>1</sup> The Rankine vortex consists of a core of solid-body rotation surrounded by an outer region of potential flow, where the tangential wind is inversely proportional to the distance from the center of circulation.

<sup>2</sup> In contrast to the Rankine vortex, the "non-Rankine vortex" may be defined as a viscous vortex that exhibits a smooth transition between solid-body rotation and potential flow, which encompasses the annular zone of the velocity maximum, resembling the Burgers–Rott (Burgers 1948; Rott 1958) tangential velocity profile.

need to examine only the cylindrical form of the cyclostrophic wind equation in azimuthal mean and integral form. This allows us to seek the factors that determine the central pressure deficit in the concentric, axisymmetric vortices of different scales. In this paper, we do not discuss the mechanisms by which the vortices are formed. Instead, we focus on the effects of the shape and distribution of the primary and secondary vortex tangential velocity profiles on tornado pressure minima. To better understand which vortex significantly contributes to the total pressure deficit, we ignore the  $V_t(r)$  term on the right-hand side in Eq. (1), replace  $V_C(r)$  by  $V_T(r)$ , take the square of  $V_C(r) = V_T(r) = V_p(r) + V_s(r)$ , and substitute the product into Eq. (2). Thus, the total radial pressure gradient force (RPGF<sub>T</sub>) due to two concentric vortices may be expressed as the sum of three centrifugal force components:

$$\text{RPGF}_T \equiv \frac{1}{\rho} \frac{\partial P_T}{\partial r} = \frac{V_p^2(r)}{r} + \frac{2V_p(r)V_s(r)}{r} + \frac{V_s^2(r)}{r}. \quad (5)$$

Physically, the term on the left-hand side of Eq. (5) represents the total acceleration due to the total radially inward-directed pressure gradient force that counterbalances with three radially outward-directed centrifugal force components associated with two concentric vortex fields. The first and third terms on the right-hand side, respectively, represent the primary centrifugal acceleration, denoted by  $V_p^2(r)/r$ , because of the primary vortex’s tangential motion and the secondary centrifugal acceleration, denoted by  $V_s^2(r)/r$ , because of the tangential motion of the secondary vortex. Comparing the first and third terms with the second term, we see that the  $2V_p(r)V_s(r)/r$  term behaves just like the centrifugal acceleration and may be interpreted as the “cross” centrifugal acceleration term influenced by the product of two different tangential velocity profiles between the primary and secondary vortex fields. The magnitudes of three individual centrifugal force terms on the right-hand side of Eq. (5) will be assessed and compared in section 6.

By integrating Eq. (5) radially inward from the environmental pressure, the total pressure deficit (PD<sub>T</sub>) due to two concentric vortices yield

$$\text{PD}_T \equiv \rho^{-1} \Delta P_T = \int_{\infty}^r \left[ \frac{V_p^2(\tau)}{\tau} + \frac{2V_p(\tau)V_s(\tau)}{\tau} + \frac{V_s^2(\tau)}{\tau} \right] d\tau, \quad (6)$$

where  $\tau$  is a dummy variable for the integration. Note that we use  $\rho \sim 1 \text{ kg m}^{-3}$  for the sake of simplicity.

Since the relative contribution of a parent mesocyclone to the low pressure at the center of a tornado has never been addressed, we propose to decompose Eqs. (5) and (6) in each component of RPGF and PD that both correspond to the primary ( $p$ ) and secondary ( $s$ ) tangential velocity profiles. They may be expressed as

$$\text{RPGF}_p \equiv \frac{1}{\rho} \frac{\partial P_p}{\partial r} = \frac{V_p^2(r)}{r} + \frac{V_p(r)V_s(r)}{r}, \quad (7a)$$

$$\text{RPGF}_s \equiv \frac{1}{\rho} \frac{\partial P_s}{\partial r} = \frac{V_s^2(r)}{r} + \frac{V_s(r)V_p(r)}{r}, \quad (7b)$$

$$\text{PD}_p \equiv \rho^{-1} \Delta P_p = \int_{\infty}^r \left[ \frac{V_p^2(\tau)}{\tau} + \frac{V_p(\tau)V_s(\tau)}{\tau} \right] d\tau, \quad (7c)$$

and

$$\text{PD}_s \equiv \rho^{-1} \Delta P_s = \int_{\infty}^r \left[ \frac{V_s^2(\tau)}{\tau} + \frac{V_s(\tau)V_p(\tau)}{\tau} \right] d\tau. \quad (7d)$$

Equations (7) will be used to calculate, plot, and compare radial profiles of RPGF and PD that slice across two concentric, axisymmetric (primary and secondary) vortices far enough aloft in a quasi-steady flow, wherever the swirl velocity is clearly dominant. This will be discussed in section 6.

### 5. A parametric tangential wind model

In this study, we chose a parametric tangential wind model of WW13, not only because of its utility and simplicity but because the one-dimensional model is valid above the tornado boundary layer, where the main swirling flow is not in cyclostrophic balance (Snow 1982; Davies-Jones 1986; Bluestein 2013; Bluestein et al. 2014). The model can be useful for parametrically constructing varying tangential velocities for different applications. Wood and Brown (2011) have shown utility in creating different parametric tangential wind profiles to investigate how the simulated Doppler tornadic vortex signatures might change as the simulated radar scanned azimuthally across the tornado structure consisting of one or two cells. For tropical cyclone applications, Wood et al. (2013) tailored the WW13 model to depict representative surface pressure profiles deduced from single-, dual-, and triple-maximum concentric-eyewall wind profiles associated with the primary (inner), secondary (first outer), and tertiary (second outer) complete rings of enhanced radar reflectivity. Kato et al. (2015) used mean anemometer data of a

near-surface, winter tornadic vortex to compare radial profiles of observed tangential winds to those of the Rankine, Burgers–Rott, and WW13 models.

*a. Parametric vortex with a single-maximum tangential velocity profile*

The WW13 profile for inviscid, axisymmetric tangential flow is expressed by

$$V(r; \mathbf{m}) = V_x \phi(r; \mu_i, \mu_o, \lambda), \quad \beta \equiv r/R_x, \quad 0 \leq r \leq \infty, \quad (8a)$$

where

$$\phi(r; \mu_i, \mu_o, \lambda) = \frac{(\mu_i - \mu_o)^\lambda \beta^{\mu_i}}{[\mu_i \beta^{(\mu_i - \mu_o)/\lambda} - \mu_o]^\lambda}, \quad \mu_i \geq 1, \quad \mu_o < 0, \quad \lambda > 0. \quad (8b)$$

Here,  $V_x$  is the maximum tangential velocity that occurs at the vortex radius  $R_x$ ,  $r$  is the radius from the vortex center, and  $\beta$  is the dimensionless vortex radius. Furthermore,  $\phi$  is the dimensionless function that employs a model vector of three shape parameters:  $\mathbf{m} = (\mu_i, \mu_o, \lambda)^T$ . The parameters shape different segments of the velocity profile. By definition,  $\mu_i$  predominantly dictates the inner (subscript  $i$ ) segment

of tangential velocity near the vortex center (e.g., one- or two-celled structure),  $\mu_o$  primarily governs the outer (subscript  $o$ ) segment beyond  $R_x$  (e.g., decay), and  $\lambda$  controls the radial width of the velocity segment straddling the velocity maximum (e.g., sharply or broadly peaked).

WW13 demonstrated that the non-Rankine vortex's tangential velocity profiles coincide with the inner and outer profiles of the Rankine tangential velocity ( $V_R$ ) by taking the limit of Eq. (8) as  $\lambda \rightarrow 0$ , regardless of the variables  $\mu_i$  and  $\mu_o$ . For an idealized Rankine vortex, we set  $\mu_i = 1$  and  $\mu_o = -1$  so that the tangential velocity profile is given by

$$V_R(r) = \begin{cases} V_{R_x} \beta_R^{\mu_i} = V_{R_x} \beta_R, & \beta_R \leq 1, \\ V_{R_x} \beta_R^{\mu_o} = V_{R_x} \beta_R^{-1}, & \beta_R \geq 1, \end{cases} \quad (9)$$

where  $\beta_R \equiv r/R_{R_x}$  is the normalized core radius and the subscript  $R$  represents Rankine. The definitions of  $\mu_i$  and  $\mu_o$  for the non-Rankine vortex are the same as those for the Rankine vortex. The radial distribution of the single Rankine vortex's pressure deficit ( $PD_R$ ), via Eq. (9), is obtained by integrating Eq. (2) radially inward from the environmental pressure and is given by

$$PD_R = \rho^{-1} \Delta P_R(r) \equiv \begin{cases} V_{R_x}^2 \left( \frac{\beta_R^{2\mu_i}}{2\mu_i} + \frac{\mu_i - \mu_o}{2\mu_i \mu_o} \right) = V_{R_x}^2 \left( \frac{\beta_R^2}{2} - 1 \right), & \beta_R \leq 1, \\ V_{R_x}^2 \frac{\beta_R^{2\mu_o}}{2\mu_o} = -\frac{V_{R_x}^2}{2\beta_R^2}, & \beta_R \geq 1, \end{cases} \quad (10)$$

The axial pressure deficit of the Rankine vortex is given by  $\rho^{-1} \Delta P_R(r) = -V_{R_x}^2$ . Both Eqs. (9) and (10) will be used to calculate and plot radial profiles of the Rankine vortex's single-maximum tangential velocity and deduced pressure deficit for comparing to those of the dual-maxima tangential velocity and inferred pressure deficit. The results will be presented in section 6.

*b. Parametric vortices with dual-maxima tangential velocity profiles*

In Eqs. (1)–(7), the  $V_p(r)$  and  $V_s(r)$  tangential velocity profiles each can be parametrically constructed, via Eq. (8), and are expressed by

$$V_p(r) = V_{px} \frac{(\mu_{pi} - \mu_{po})^{\lambda_p} \beta_p^{\mu_{pi}}}{[\mu_{pi} \beta_p^{(\mu_{pi} - \mu_{po})/\lambda_p} - \mu_{po}]^{\lambda_p}}, \quad \beta_p \equiv r/R_{px}, \quad 0 \leq r \leq \infty, \quad (11a)$$

and

$$V_s(r) = V_{sx} \frac{(\mu_{si} - \mu_{so})^{\lambda_s} \beta_s^{\mu_{si}}}{[\mu_{si} \beta_s^{(\mu_{si} - \mu_{so})/\lambda_s} - \mu_{so}]^{\lambda_s}}, \quad \beta_s \equiv r/R_{sx}, \quad 0 \leq r \leq \infty, \quad (11b)$$

provided that  $V_{sx} < V_{px}$ . Each single-maximum tangential wind profile must be approximated by continuous, nonzero mathematical functions that are zero (i.e.,  $\mathbf{m} \neq 0$ ) at a vortex center, increase to its vortex radius ( $R_x$ ) at which a single-maximum tangential velocity ( $V_x$ ) occurs, and decrease to zero asymptotically at radial infinity, with different functions shaping different portions of the velocity profile. When two profiles of  $V_p(r)$  and  $V_s(r)$  are added, a new (total) profile having a dual-maxima tangential wind structure is obtained. The superposition of two profiles is much easier to work with than one dual-maxima tangential wind profile that may

TABLE 1. Profile parameters that produced the radial profiles of the primary (*p*) and secondary (*s*) tangential velocities ( $\text{m s}^{-1}$ ) for eight experiments (A–H). The units of vortex radii ( $R_{px}$  and  $R_{sx}$ ) are km; the shape parameters of  $\mu_r$ ,  $\mu_o$ , and  $\lambda$  are dimensionless. Note that boldface numbers with a horizontal arrow represent a change in parameter value in each experiment, except for experiment A.

Expt	Primary vortex					Secondary vortex				
	$V_{px}$	$R_{px}$	$\mu_{pi}$	$\mu_{po}$	$\lambda_p$	$V_{sx}$	$R_{sx}$	$\mu_{si}$	$\mu_{so}$	$\lambda_s$
A	100	0.2	1	−1	$10^{-2}$	25	2	1	−1	$10^{-2}$
B	100	0.2	1	−1	$10^{-2}$	<b>25</b> → <b>50</b>	2	1	−1	$10^{-2}$
C	100	0.2	1	−1	$10^{-2}$	50	<b>2</b> → <b>1</b>	1	−1	$10^{-2}$
D	100	<b>0.2</b> → <b>0.1</b>	1	−1	$10^{-2}$	50	<b>2</b> → <b>1</b>	1	−1	$10^{-2}$
E	100	0.2	1	−1	$10^{-2}$	50	2	1	<b>−1</b> → <b>−0.2</b>	$10^{-2}$
F	100	0.2	1	−1	$10^{-2}$	50	2	1	−1	<b><math>10^{-2}</math></b> → <b>0.5</b>
G	100	0.2	1	−1	<b><math>10^{-2}</math></b> → <b>1</b>	50	2	1	−1	$10^{-2}$
H	35	2	1	−1	$10^{-2}$	<b>20</b> → <b>30</b>	0.1	1	−1	$10^{-2}$

be difficult to formulate, because the latter profile must be estimated by continuous functions that shape different segments encompassing the first and second wind-maximum wind profile.

### 6. Comparative results

This section uses Eq. (11) to construct and superposition two different radial profiles of the tangential winds aloft in the outer-flow region. To provide what each input parameter may be able to deduce about the primary and secondary tangential wind and deduced pressure deficit structures, Table 1 lists the selected input parameter values for creating each Rankine tangential wind profile for the primary and secondary circulations in eight experiments. In each experiment (except for experiment A), we perform comparative cases by varying one parameter (boldface number) while keeping other parameters unchanged in the radial distributions of the tangential velocities. Since these parameters are not known in reality, the input parameters for this and other simulations are purely subjective in order to keep the one-dimensional Rankine and non-Rankine models and a mathematical analysis as simple as possible for the sake of interpretation. In all experiments, the constant  $\mu_i$  values of 1.0 concur with the findings of Wurman and Gill (2000), Wurman (2002), Wurman and Alexander (2005), Kosiba et al. (2014), and Kato et al. (2015), wherein the Rankine tangential winds approximated the inner cores of solid-body rotation (i.e.,  $V \propto r^{\mu_i}$ , where  $\mu_i \sim 1$ )—in some cases to the inner radial profiles of Doppler velocities. Our approach presented here was similar to that of Knaff et al. (2011) and Wood et al. (2013), who investigated the influences of fine-tuning the different parameters on their different models of tropical cyclone intensity, strength, and size that can impact a tropical cyclone’s central pressure minima.

#### a. Experiment A

A simple experiment A is presented in Fig. 3, wherein a smaller-scale, primary vortex representing a tornado is located at the center of a larger-scale, secondary vortex representing a supercell mesocyclone in the outer-flow region. The radial profiles of Rankine tangential velocity, deduced pressure deficit, and radial pressure gradient force associated with the primary and secondary Rankine vortices are constructed from the selected parameters given in Table 1, via Eqs. (5)–(11), and are plotted in Fig. 3. To represent some of the variety found in nature, we assume a strong tornado characteristic of its maximum tangential velocity ( $V_{px} = V_{R_x}$ ) of  $100 \text{ m s}^{-1}$  at its vortex radius ( $R_{px} = R_{R_x}$ ) of 200 m (red curve). Using Eq. (10), the central pressure deficit deduced from the Rankine tangential velocity profile alone is  $-100 \text{ hPa}$  (gray curve), in this experiment and subsequent experiments (except for experiment H) for comparison. At the same time, a supercell mesocyclone (blue curve) has its vortex radius ( $R_{sx}$ ) of 2000 m, where its maximum tangential velocity ( $V_{sx}$ ) of  $25 \text{ m s}^{-1}$  occurs. When the profiles of  $V_p$  and  $V_s$  are superposed, the “observed” (total) profile of  $V_T$  (black curve) is produced. The co-existence of the concentric, primary, and secondary vortices yields a dual tangential wind maxima and a saddle-shaped wind minimum (black curve) and also results in the “observed” (total) deduced pressure minimum (black curve of  $\text{PD}_T = \text{PD}_p + \text{PD}_s$  in Fig. 3b). This minimum is greater than the single Rankine’s central pressure deficit of  $\text{PD}_R$  of  $-100 \text{ hPa}$ , because the combined primary and secondary vortices, respectively, contribute  $\text{PD}_p = -108 \text{ hPa}$  and  $\text{PD}_s = -15 \text{ hPa}$  to the  $\text{PD}_T$  value of  $-123 \text{ hPa}$  (Table 2). The more (less) significant contribution is from the primary (secondary) vortex, accounting for 88% (12%) of  $\text{PD}_T$ . It is suggested that the “observed” central pressure minimum (black curve) due to the tornado alone may be overestimated,

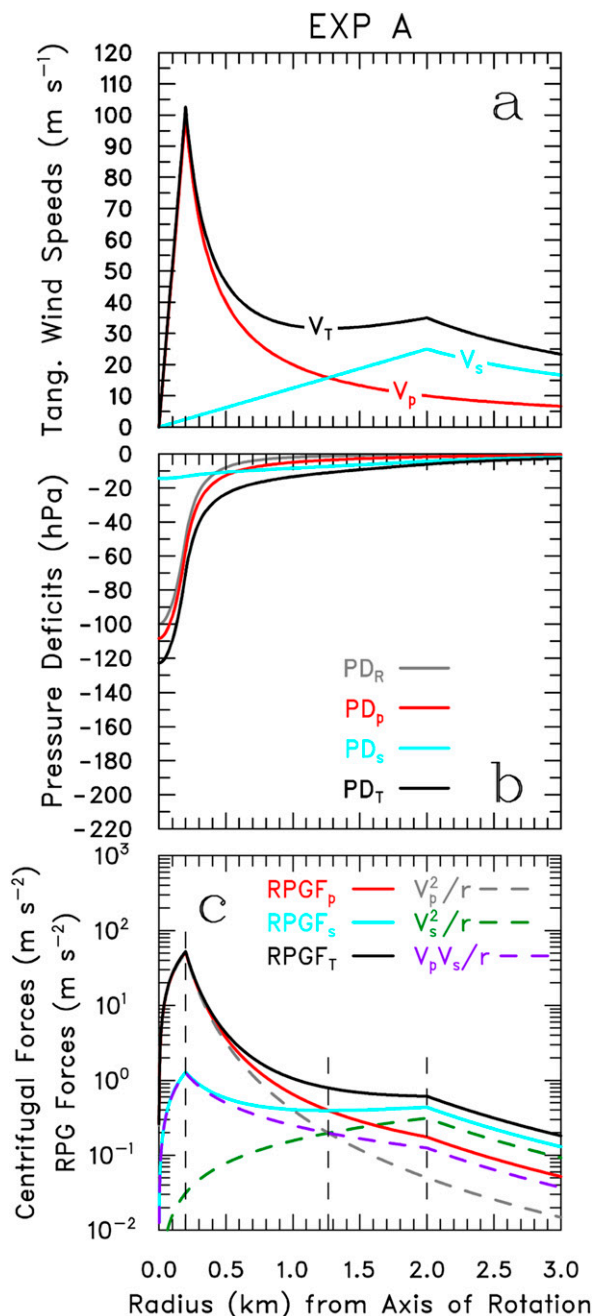


FIG. 3. Radial distributions of (a) primary ( $V_p$ , red curve), secondary ( $V_s$ , blue curve), and total ( $V_T$ , black curve) Rankine tangential wind speeds ( $\text{m s}^{-1}$ ); (b) single Rankine ( $PD_R$ , gray curve), primary ( $PD_p$ , red curve), secondary ( $PD_s$ , blue curve), and total ( $PD_T$ , black curve) pressure deficits (hPa); and (c) primary ( $RPGF_p$ , red solid curve), secondary ( $RPGF_s$ , blue solid curve), and total ( $RPGF_T$ , black solid curve) radial pressure gradient forces ( $\text{m s}^{-2}$ ) corresponding to the primary and secondary centrifugal forces as a function of radius ( $r$ , km) from the axis of rotation for experiment A. In (c), the gray and green dashed curves represent the primary ( $V_p^2/r$ ) and secondary ( $V_s^2/r$ ) centrifugal forces, respectively. The purple dashed curve represents the enhanced ( $V_p V_s/r$ ) centrifugal force. The left, middle, and right vertical dashed lines are described in the text.

compared to the single Rankine's central pressure deficit (gray curve). This is owing to the fact that the secondary vortex may have an impact on the behavior of the total pressure deficit, even if the primary and secondary vortices' wind and deduced pressure deficit structures remain unchanged. If the secondary vortex were nonexistent (i.e.,  $V_s = 0$ ), the contribution of the primary vortex's maximum tangential velocity to the central pressure deficit would have been 100% (gray curve), as expected.

We explore the role of the centrifugal force components in Eqs. (7a) and (7b) in the physical behavior of the radial pressure gradient force components in the primary and secondary vortices. The individual centrifugal acceleration components corresponding to the solid curves of  $V_p$  (red),  $V_s$  (blue), and  $V_T$  (black) are presented in Fig. 3c. The radial profiles of  $RPGF_p (= V_p^2/r + V_p V_s/r)$ ,  $RPGF_s (= V_s^2/r + V_p V_s/r)$ , and "observed" (total)  $RPGF_T (= V_p^2/r + 2V_p V_s/r + V_s^2/r)$ , respectively, are indicated by the red, blue, and black curves. When the red and blue curves intersect at approximately  $r = 1.27$  km, a vertical (middle) dashed line may separate the primary and secondary vortices. To the left of the line, the primary radial pressure gradient force ( $RPGF_p$ ) dominates the secondary radial pressure gradient force ( $RPGF_s$ ), because the primary centrifugal force ( $V_p^2/r$ ) closer to the circulation axis is always stronger than the secondary one ( $V_s^2/r$ ) far away from the axis as both the forces vary inversely proportional to the radius ( $1/r$ ) from the axis. At the same time, the  $RPGF_s$  dominates the  $RPGF_p$  to the right of the line. Beyond  $R_{px}$  and  $R_{sx}$ , the radial distributions of  $RPGF_p$  and  $RPGF_s$ , respectively, decrease asymptotically to zero at radial infinity. If the secondary vortex were absent (i.e.,  $V_s = 0$ ), the  $V_p V_s/r$  term would have vanished so that the primary centrifugal force would have been reduced to only a single Rankine vortex's centrifugal force (gray, dashed curve in Fig. 3c).

The magnitudes of three individual centrifugal force terms of  $V_p^2/r$ ,  $V_p V_s/r$ , and  $V_s^2/r$  may be assessed and compared by setting  $V_p = V_{px}$  at  $r = R_{px}$  and also  $V_s = V_{sx}$  at  $r = R_{sx}$ . The results are given in Table 3. Note that the largest  $V_p V_s/r$  term at  $r = R_{px}$  (indicated by a left, vertical dashed line in Fig. 3c) is always less than the largest  $V_p^2/r$  term but greater than the largest  $V_s^2/r$  term. Conversely, the largest  $V_p V_s/r$  term at  $r = R_{sx}$  (also indicated by a right, vertical dashed line) is always greater than the largest  $V_p^2/r$  term but less than the largest  $V_s^2/r$  term. Furthermore, the contribution of  $V_p^2/r$  to the central pressure deficit is much greater (less) than that of  $V_s^2/r$  at  $r = R_{px}$  ( $R_{sx}$ ), because  $V_{px} > V_{sx}$  and also because both primary and secondary centrifugal forces vary inversely proportional to the radius from the circulation center. At the same time, the contribution of the largest

TABLE 2. Central primary (PD<sub>p</sub>, hPa) and secondary (PD<sub>s</sub>, hPa) pressure minima and relative contributions (%) of PD<sub>p</sub> and PD<sub>s</sub> to the total central pressure deficits (PD<sub>T</sub>, hPa) for eight experiments (A–H). A horizontal arrow represents a change in parameter values (from lightface to boldface numbers). A symbol Δ represents a difference in the central pressure deficit (hPa) when the change in parameter values occurs. Note that the percentage (%) is calculated as 100 × PD<sub>p</sub>/PD<sub>T</sub> for the primary vortex and also 100 × PD<sub>s</sub>/PD<sub>T</sub> for the secondary vortex.

Expt	Primary vortex			Secondary vortex			PD <sub>T</sub>	Δ
	PD <sub>p</sub>	Δ	%	PD <sub>s</sub>	Δ	%		
A	−108	0	88	−15	0	12	−123	0
B	−108 → <b>−117</b>	−9	88 → <b>74</b>	−15 → <b>−41</b>	−26	12 → <b>26</b>	−123 → <b>−158</b>	−35
C	−117 → <b>−126</b>	−9	74 → <b>71</b>	−41 → <b>−51</b>	−10	26 → <b>29</b>	−158 → <b>−177</b>	−19
D	−117 → <b>−117</b>	0	74 → <b>74</b>	−41 → <b>−41</b>	0	26 → <b>26</b>	−158 → <b>−158</b>	0
E	−117 → <b>−118</b>	−1	74 → <b>56</b>	−41 → <b>−92</b>	−51	26 → <b>44</b>	−158 → <b>−210</b>	−52
F	−117 → <b>−122</b>	−5	74 → <b>67</b>	−41 → <b>−62</b>	−21	26 → <b>33</b>	−158 → <b>−184</b>	−26
G	−117 → <b>−228</b>	−111	74 → <b>81</b>	−41 → <b>−53</b>	−12	26 → <b>19</b>	−158 → <b>−281</b>	−123
H	−13.7 → <b>−14.4</b>	−0.7	72 → <b>56</b>	−5.4 → <b>−11.2</b>	−5.8	28 → <b>44</b>	−19.1 → <b>−25.6</b>	−6.5

$V_p V_s / r$  term at  $r = R_{px}$  to the central pressure deficit is greater than that at  $r = R_{sx}$ . It is suggested that the mesocyclone’s largest centrifugal force ( $V_s^2 / r$ ) at  $R_{sx}$  may be too small to influence the tornado vortex structure, even though the tornado’s wind and pressure structures remain largely unchanged.

b. Experiment B

What would happen to a central pressure minimum if the mesocyclone experiences increasing intensity from its maximum tangential wind speed of 25–50 m s<sup>−1</sup> (magenta, upward-pointing arrow in Fig. 4a)? As expected, an increase in  $V_{sx}$  (Table 1) is strongly correlated with vortex intensity and a large central pressure minimum when other free model parameters for depicting the primary and secondary tangential velocity profiles are held constant for experiment B. The central pressure minimum associated with the primary vortex falls from −108 to −117 hPa, even though the tornado’s wind structure does not change at all. At the same time, the central pressure minimum associated with the secondary vortex drops from −15 to −41 hPa. While the red (solid) PD<sub>p</sub> curve does not change appreciably (Fig. 4b) and is closely parallel to the gray PD<sub>R</sub> curve, the blue, solid PD<sub>s</sub> curve falls significantly, because an increase in  $V_{sx}$  contributes −41 hPa to a large minimum of PD<sub>T</sub> = −158 hPa (black, solid curve) at the vortex center. Table 2 quantifies the relative contributions of the primary and secondary vortices to the total central pressure deficits and also the differences in the central pressure deficits and percentages when the change in parameter values occurs for this experiment. For instance, the contribution of the increase in  $V_{sx}$  to the central PD<sub>T</sub> increased from 12% to 26%, while, at the same time, the increase in  $V_{sx}$  reduced PD<sub>T</sub> from −123 to −158 hPa by 35 hPa. Even though the primary tornado wind (red curve in Fig. 4a) and pressure (gray

curve in Fig. 4b) structures do not change, the contribution of the increase in  $V_{sx}$  to the central PD<sub>p</sub> decreased from 88% to 74% (from −108 to −117 hPa). This is because the inner profile of  $V_s$ , shown by the second term on the right-hand side of Eq. (7a), influences the inner profile of  $V_p V_s / r$ .

As the mesocyclone’s maximum tangential wind speed is increased, the vertical dashed line separating the region where RPF<sub>p</sub> is dominant from the dominant region of RPF<sub>s</sub> is shifted toward the vortex center (Fig. 4c). The shift corresponds to increased centrifugal forces in association with the intensifying secondary vortex, as a comparison between Figs. 3c and 4c illustrates.

c. Experiment C

Lee and Wurman (2005), Knaff et al. (2011), and WW13 showed that for a given maximum tangential wind speed, a central pressure minimum was relatively insensitive to variations in a single vortex’s vortex radius at which the maximum occurs. This insensitivity raises an important question about whether the vortex radius variation affects a central pressure minimum when a primary (tornado) vortex is centered within a secondary

TABLE 3. Assessment of the magnitudes of three individual centrifugal force terms (m s<sup>−2</sup>) associated with the primary (secondary) Rankine tangential velocity maximum at  $r = R_{px}$  ( $R_{sx}$ ), using the selected parameters in Table 1 for experiment A.

	At $r = R_{px}$	At $r = R_{sx}$
$\frac{V_p^2}{r}$	$\frac{V_{px}^2}{R_{px}} = 50.00$	$\frac{V_{sx}^2 R_{px}^2}{R_{sx}^3} = 0.05$
$\frac{V_p V_s}{r}$	$\frac{V_{px} V_{sx}}{R_{sx}} = 1.25$	$\frac{V_{px} V_{sx} R_{px}}{R_{sx}^2} = 0.13$
$\frac{2V_p V_s}{r}$	$\frac{2V_{px} V_{sx}}{R_{sx}} = 2.50$	$\frac{2V_{px} V_{sx} R_{px}}{R_{sx}^2} = 0.25$
$\frac{V_s^2}{r}$	$\frac{V_{sx}^2 R_{px}}{R_{sx}^2} = 0.03$	$\frac{V_{sx}^2}{R_{sx}} = 0.31$

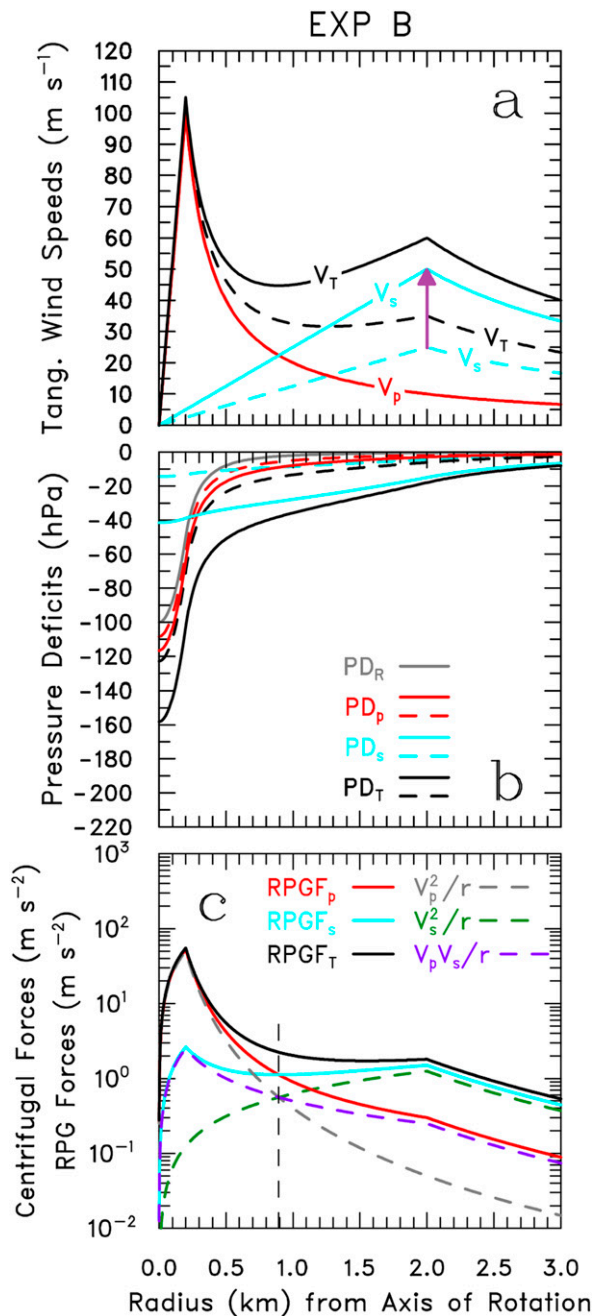


FIG. 4. As in Fig. 3, but (a) with the magenta arrow showing that  $V_s$  has increased from 25 to  $50 \text{ m s}^{-1}$  with the blue (black) solid and dashed  $V_s$  ( $V_T$ ) curves for experiment B. (b) The solid and dashed curves are indicated when the arrow shows which parameter was varied in (a). The radial distribution of the Rankine pressure deficit ( $PD_R$ ) deduced from the Rankine tangential wind speed (red curve) is indicated by a gray curve for comparison. In (a) and (b), the dashed curves are identical to the solid curves in Figs. 3a and 3b. (c) Solid curves represent radial pressure gradient forces and dashed curves represent centrifugal forces. The gray and green dashed curves represent the primary ( $V_p^2/r$ ) and secondary ( $V_s^2/r$ ) centrifugal forces, respectively. The purple dashed curve represents the enhanced ( $V_p V_s/r$ ) centrifugal force. Note that the color curves in (c) correspond to the solid curves in (a) and (b). Vertical dashed lines at  $r = R_{px}$  and  $R_{sx}$  are removed.

(mesocyclone) vortex. To answer the question, we ran another experiment (experiment C) in which the primary and secondary wind structures remained unchanged (Table 1), except that the secondary vortex is contracted by halving  $R_{sx}$  (horizontal, magenta arrow in Fig. 5a). For a given secondary tangential velocity maximum ( $V_{sx}$ ), the decrease in  $R_{sx}$  decreases the central  $PD_T$  from  $-158$  to  $-177 \text{ hPa}$  (Table 2), reducing the pressure by  $19 \text{ hPa}$ . The primary (secondary) vortex's central pressure minimum falls slightly from  $-117$  to  $-126 \text{ hPa}$  ( $-41$  to  $-51 \text{ hPa}$ ), as a comparison between the red (blue) solid and dashed curves in Fig. 5b illustrates. When the secondary vortex has contracted to the small vortex size, the secondary vortex contributes slightly more to the total central pressure deficit than the primary vortex does. The striking feature in Fig. 5b is that pressure decreased (increased) everywhere to the left (right) of a vertical dashed line located at approximately  $r = 0.62 \text{ km}$ . The line separates one region where  $RPGF_p$  is dominant from the other dominant region of  $RPGF_s$ . Apparently, the secondary vortex's centrifugal acceleration component is increased by shifting the pointed curves from  $r = 2$  to  $r = 1 \text{ km}$ , when comparing between Figs. 4c and 5c. For given values of  $V_{px}$  and  $V_{sx}$ , the central pressure minima in the dual-vortex composite appear to be relatively sensitive to variations in the secondary vortex's vortex radius only when the primary vortex's wind and pressure structures remain unchanged.

#### d. Experiment D

In the last paragraph, we demonstrated that only the secondary vortex was displaced inward toward the vortex center, while, at the same time, the primary vortex's position remained fixed. Now, we conduct another experiment (experiment D) by varying both the primary and secondary vortex radii to determine whether the change in vortex radii can impact a central pressure minimum. If we reduce  $R_{px}$  and  $R_{sx}$  (Table 1) by one-half (i.e.,  $R_{px} = R_{px}/2$  and  $R_{sx} = R_{sx}/2$ ), then the primary and secondary vortex radii contract, as indicated by the small and large magenta arrows connecting the pointed profiles of  $V_p$  and  $V_s$  (dashed curves) to those (solid curves) in Fig. 6. It is evident that for given values of  $V_{px}$  and  $V_{sx}$ , the central pressure minima ( $PD_p$ ,  $PD_s$ ,  $PD_T$ ) are identical (Table 2), because the minima are relatively insensitive to variations in the vortex radii where  $V_{px}$  and  $V_{sx}$  occur. However, the pressure increased everywhere beyond the vortex center.

#### e. Experiment E

Based on proximity radar observations of tornadoes by mobile, high-resolution Doppler radars, the modified

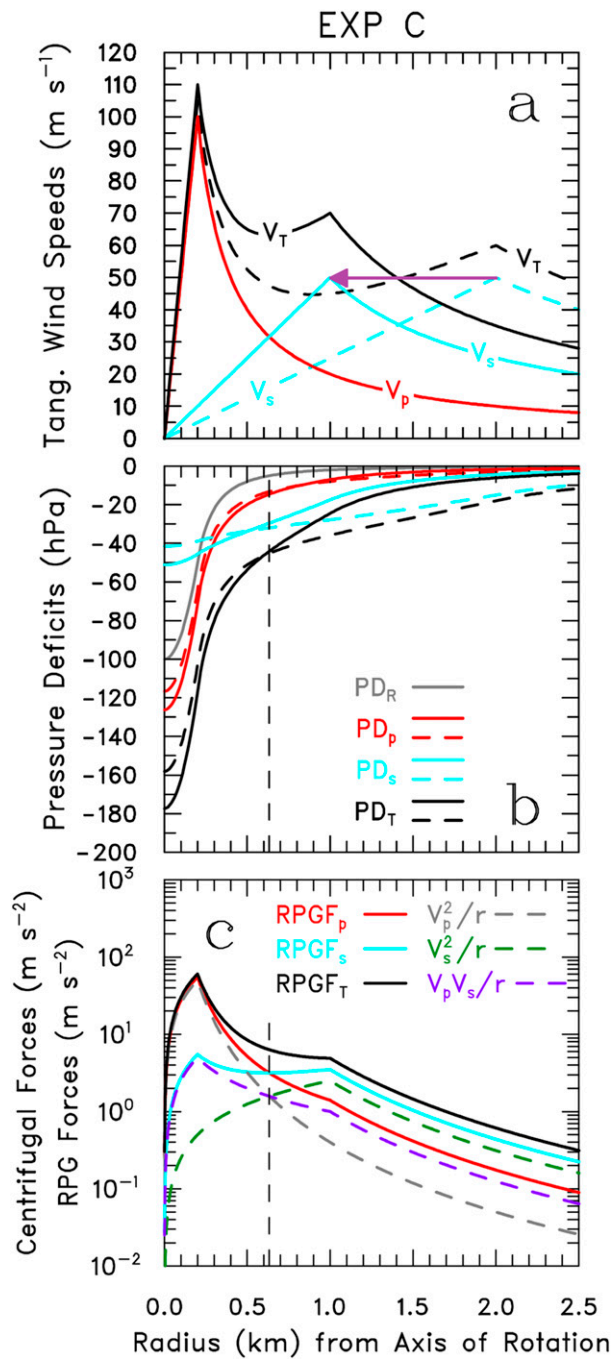


FIG. 5. As in Fig. 4, but for experiment C. In (b), the vertical dashed line is described in text.

Rankine tangential winds approximated the outer radial profiles of tangential velocities outside the radius of maximum winds, using  $V \propto r^{\mu_o}$ , where  $\mu_o = -0.6 \pm 0.1$  (Wurman and Gill 2000; Wurman 2002; Wurman and Alexander 2005). Kosiba et al. (2014) suggested that the outer modified the Rankine tangential winds outside the radius of maximum winds ( $\mu_o = -0.8 \pm 0.1$ ) on the basis

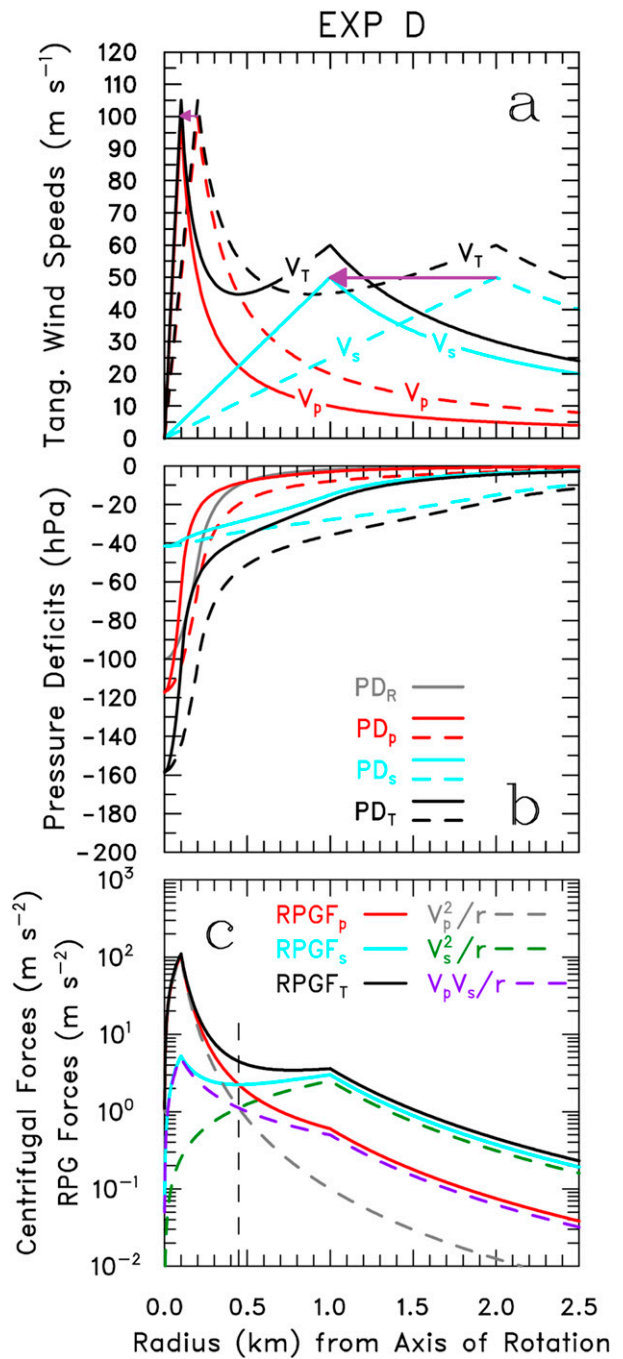


FIG. 6. As in Fig. 4, but for experiment D.

of lidar Doppler velocity and anemometer data. Kato et al. (2015) used wind speed and direction measurements from anemometer data to fit to outer tangential wind profiles in a modified Rankine vortex ( $\mu_o = -0.5 \pm 0.1$ ).

Now, we begin to explore the role of the decay parameter ( $\mu_{so}$ ) in influencing the outer profile of the velocity beyond  $R_{sx}$ , where a change in  $\mu_{so}$  is illustrated for experiment E (Table 1 and Fig. 7). A decrease in  $\mu_{so}$

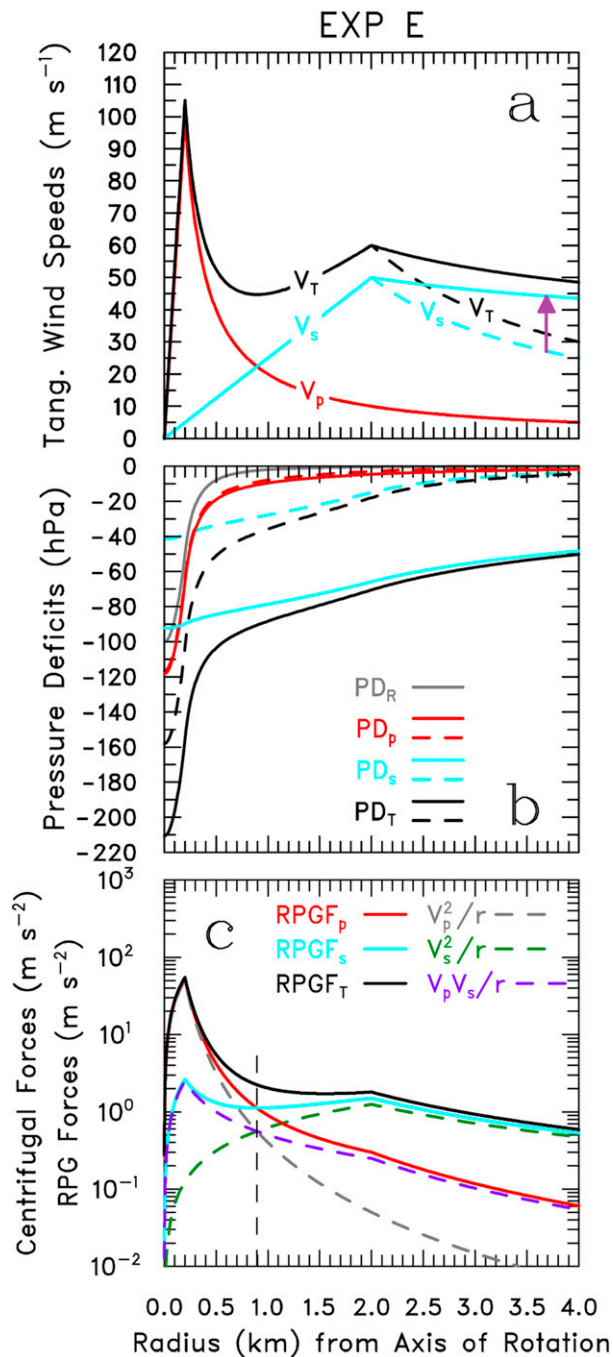


FIG. 7. As in Fig. 4, but for experiment E.

produces a slow decrease in  $V_s$  with increasing radius. Also, the decay parameter affects the outer profile of  $\text{RPGF}_s$  that corresponds to the outer  $V_p$  and  $V_s$  profiles, which is responsible for increasing the  $\text{PD}_s$  pressure deficit without affecting the  $\text{PD}_p$  profile appreciably. The decay parameter can greatly affect a central pressure minimum associated with the secondary vortex, because the quantity being integrated with respect to  $\tau$  [Eqs. (7c)

and (7d)] to get a large central pressure minimum in association with the secondary vortex is greater than that associated with the primary vortex. The secondary vortex's central pressure minimum, for instance, dramatically falls from  $-41$  to  $-92$  hPa, whereas the primary vortex's central pressure minimum insignificantly decreases from  $-117$  to  $-118$  hPa (Table 2). Concurrently, the total central pressure minimum ( $\text{PD}_T$ ) significantly decreases from  $-158$  to  $-210$  hPa. The contribution of the decrease in  $\mu_{s0}$  to the central  $\text{PD}_T$  increased from 26% to 44%.

#### f. Experiment F

The azimuthal profile of the Doppler velocities (Fig. 2) reveals that there are two types of tangential velocity segments straddling the velocity maximum: 1) sharply peaked and 2) broadly peaked. To demonstrate how  $\lambda$  changes the radial width of the velocity segment in association with the secondary vortex, we conducted another experiment (experiment F) by increasing  $\lambda_s$  from 0.01 to 0.5 (Table 1). Such an increase transforms the sharply peaked profile of the secondary Rankine tangential velocity into a broadly peaked profile of the secondary non-Rankine tangential velocity (Fig. 8). Concurrently, the change in  $\lambda_s$  causes the secondary pressure deficit  $\text{PD}_s$  to deepen, thereby contributing to the magnitude of  $\text{PD}_T$ . Also, the transition does not change the magnitude of  $\text{PD}_p$  appreciably (Table 2).

The salient feature in Fig. 8c is the change from the sharply to the broadly peaked profiles of centrifugal forces in association with the transitioning secondary vortex, when compared with Fig. 4c. The vertical dashed line is slightly shifted from 0.9 to 0.75 km. Contributions in calculated percentages and values of  $\text{PD}_p$  and  $\text{PD}_s$  to  $\text{PD}_T$  for experiment F are tabulated in Table 2.

#### g. Experiment G

In the examples presented thus far, we have shown how the  $\lambda$  parameter modifies the velocity segment of the secondary tangential velocity, which, in turn, alters the pressure deficit structure. A key question to be addressed is: What would happen to a central pressure minimum if the primary Rankine wind structure is changed into a primary non-Rankine wind structure, while, at the same time, the secondary Rankine wind structure remains unchanged? In experiment G, we chose to change  $\lambda_p$  from  $10^{-2}$  to 1 in the primary tangential velocity profile, while keeping other primary input parameters constant (Table 1 and Fig. 9). The resultant broadly peaked tangential velocity profile and corresponding centrifugal forces in association with the non-Rankine primary vortex have a larger central pressure deficit, compared to that associated with the Rankine vortex (red, solid curve

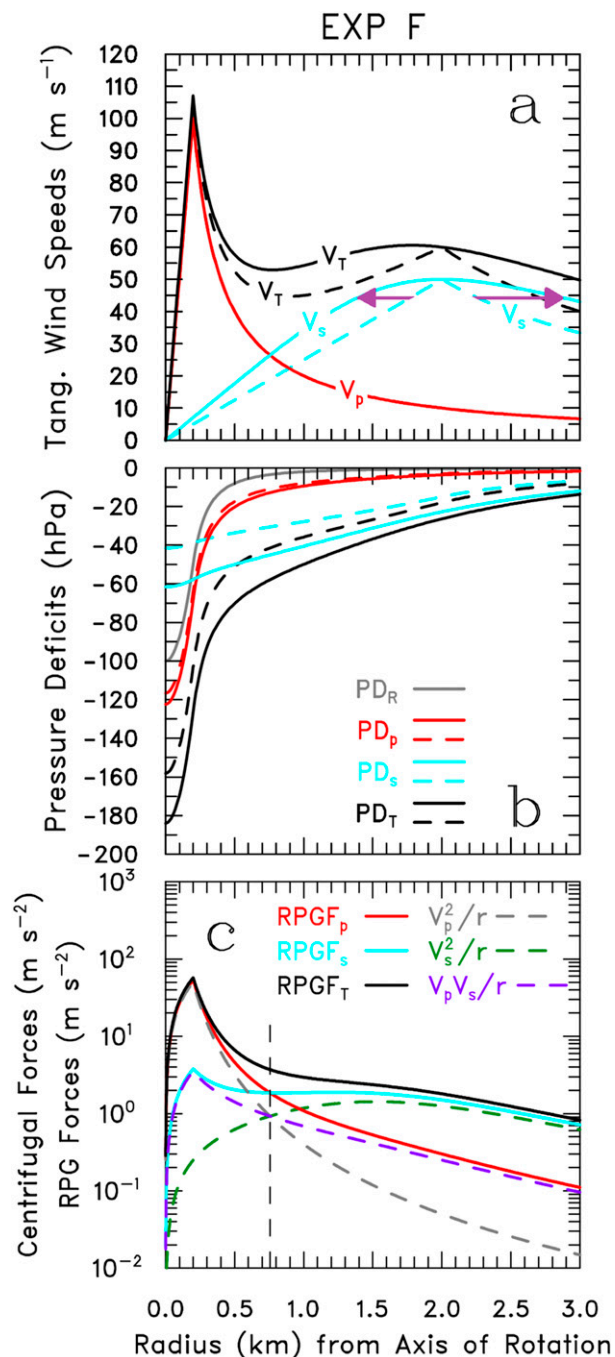


FIG. 8. As in Fig. 4, but for experiment F.

in Fig. 4b). Furthermore, the maximum radial pressure gradient associated with the primary vortex inside  $R_{px}$  is shifted toward the radius where the primary centrifugal force maximum occurs.

*h. Experiment H*

In the last several subsections, we have discussed the influences of larger-scale, secondary vortex variability on

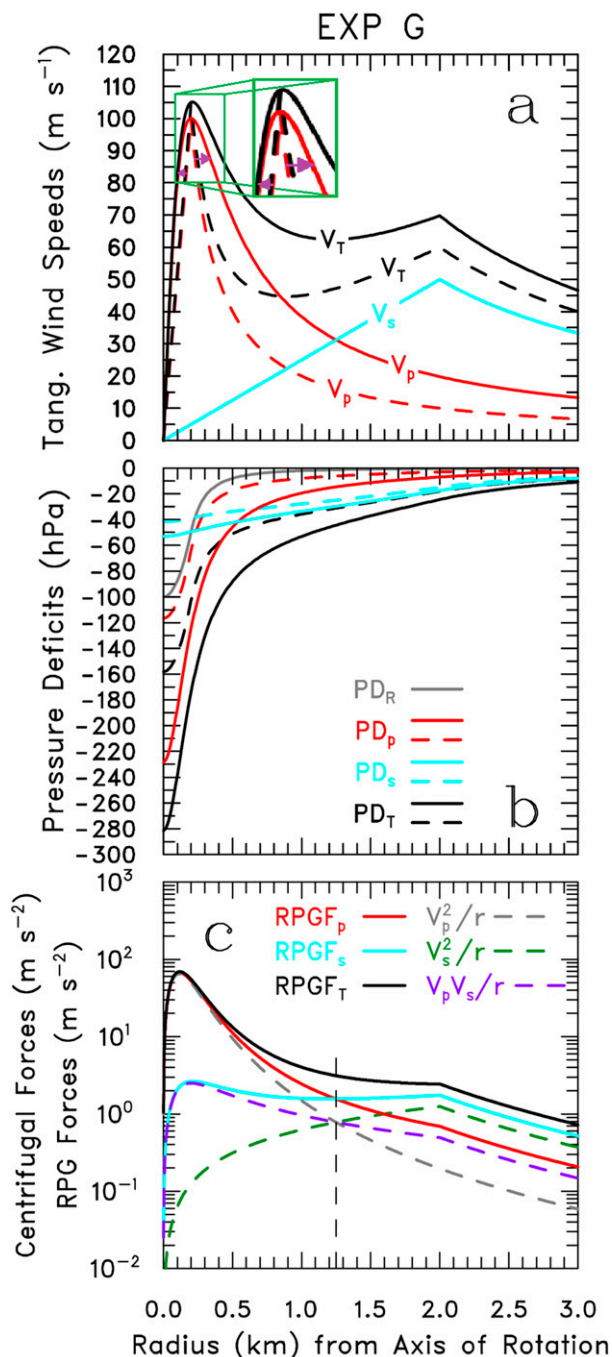


FIG. 9. As in Fig. 4, but for experiment G. In (a), a green rectangle illustrating the radial width of the tangential velocity profile straddling the velocity maximum is enlarged for ease of readability.

tornado pressure minima when the primary (tornado) vortex's wind structure remained unchanged. Now, we reverse all the previous experiments A–G by stating that in another and final experiment H, a strong mesocyclone is now the primary vortex and a weak tornado is now the secondary vortex. In this experiment, we explore the

effects of smaller-scale vortex variability on tornado pressure minima when the tornado, as a smaller-scale, separate vortex, is centered within the steady-state mesocyclone. Tanamachi et al. (2013) described the collection of high-resolution, W-band Doppler radar data in a sub-tornado-strength, convective vortex (SCV) that occurred near Prospect Valley, Colorado, on 26 May 2010 as part of the Second Verification of the Origins of Rotation in Tornadoes Experiment (VORTEX2; Wurman et al. 2012) field campaign. The SCV never attained wind speeds meriting designation as a tornado with a rating of EF0 on the enhanced Fujita (EF) scale (McDonald et al. 2004; WSEC 2006), but its vortex structure and evolution were suggestive of a tornado.

We used combinations of one low-level mesocyclone and two tornadoes having different velocity strengths as listed in Table 1 for experiment H. When the SCV's tangential velocity peak was assumed to be  $20 \text{ m s}^{-1}$  at its vortex radius of 100 m, the radial distributions of the tangential wind and pressure deficit in association with the primary (mesocyclone) and secondary (SCV) vortices, respectively, are indicated by the dashed curves in Figs. 10a and 10b. The red dashed curve showing  $PD_p$  associated with the primary vortex may represent a radial profile of relatively low pressure (mesolow) in association with a mature mesocyclone. The SCV's central pressure minimum was  $-5.4 \text{ hPa}$ ; at the same time, the primary vortex's central pressure minimum was  $-13.7 \text{ hPa}$ . The total central pressure minimum was  $-19.1 \text{ hPa}$ . Brooks (1949) found that tornadoes were embedded in regions of relatively low pressure whose horizontal scale was greater than that of the tornado.

Suppose that the SCV intensified into an EF0 tornado by increasing its maximum tangential wind up to  $30 \text{ m s}^{-1}$  (a magenta upward-pointing arrow in Fig. 10). Figure 10 presents the resultant profiles of tangential wind, centrifugal forces, and central pressure deficits in association with the primary and secondary vortices. The secondary vortex's central pressure deficit ( $PD_s$ ) is  $-11.2 \text{ hPa}$  (solid blue curve in Fig. 10b), compared to the single Rankine vortex's central pressure deficit ( $PD_R = -9 \text{ hPa}$ ; gray curve) that the single Rankine vortex would have in the absence of the secondary vortex. This implies that in Table 2 the intensifying secondary vortex contributes  $-11.2 \text{ hPa}$ , or about 44% of the total central pressure deficit ( $PD_T = -25.6 \text{ hPa}$ ). Simultaneously, the secondary vortex reduces the unchanged primary vortex's contribution from 72% to 56%. Additionally, the right half of the narrow V-shaped profile (blue, solid curve) of the tornado pressure minimum is embedded within the right half of the large, bowl-shaped pressure deficit

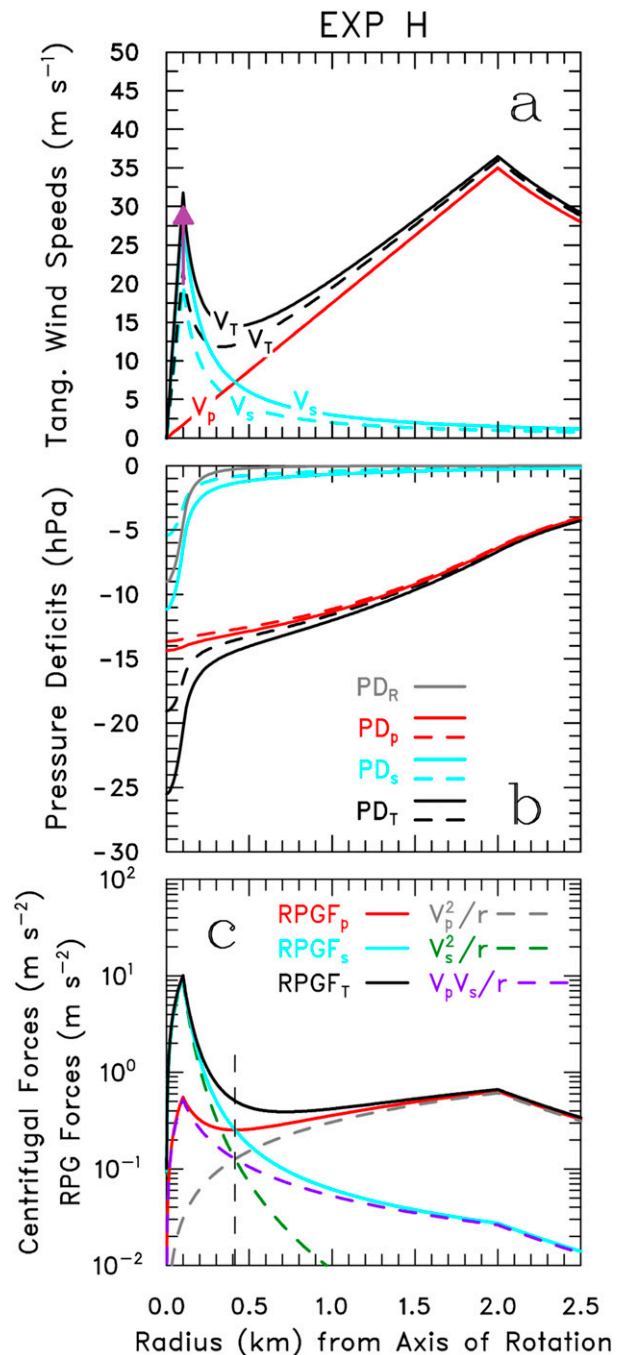


FIG. 10. As in Fig. 4, but for experiment H.

profile (red, solid curve) of the low-level mesocyclone between the vortex axis and several kilometers from the axis. The  $PD_T$  distribution (black, solid curve) resulting from the combined profiles of  $PD_p$  and  $PD_s$  bears resemblance to a surface pressure record during an intense tornado cyclone passage (e.g., Brooks 1949; Davies-Jones 1986) and also during a supercell, low-level mesocyclone passage (Karstens et al. 2010).

The centrifugal force associated with the transitioning secondary vortex is dominant between the vortex center and  $r \sim 0.4$  km (vertical dashed line in Fig. 10c). Beyond that radius, the secondary centrifugal force rapidly decreases to zero asymptotically, whereas the primary vortex's centrifugal force increases slowly up to  $R_{px}$  and then decreases to zero asymptotically to the radial infinity.

## 7. Summary and discussion

The Wood and White (2013) parametric tangential wind profile model supplemented with cyclostrophic balance and quasi-steady-state assumptions offers a diagnostic tool for depicting tangential wind and deducing pressure deficit structures in a primary vortex (e.g., tornado) centered within a secondary vortex (e.g., mesocyclone) above the tornado boundary layer. Both vortices were assumed to be concentric and axisymmetric, thus facilitating a simple mathematical analysis using the Rankine and non-Rankine vortex models. The partitioned cyclostrophic wind equations allowed us to analyze and determine the effect of one varying segment of the tangential wind profile on the deduced pressure deficit structures. The main conclusions of this study are as follows:

- 1) A change in one key velocity-controlling parameter that shapes a segment of the tangential wind profile in a tornado (mesocyclone) vortex yields significant contributions to the total central pressure deficit, even though the mesocyclone (tornado) vortex's tangential wind structure remains unchanged.
- 2) In all experiments except for experiment H, the largest  $V_p V_s / r$  term at  $r = R_{px}$  is less than the largest  $V_p^2 / r$  term but greater than the largest  $V_s^2 / r$  term. Conversely, the largest  $V_p V_s / r$  term at  $r = R_{sx}$  is greater than the largest  $V_p^2 / r$  term but less than the largest  $V_s^2 / r$  term. In experiment H where a strong mesocyclone is now the primary vortex and a weak tornado is now the secondary vortex, the orders of magnitude of the largest  $V_p V_s / r$  term comparable to the largest  $V_p^2 / r$  and  $V_s^2 / r$  terms at  $r = R_{px}$  and  $R_{sx}$  are now opposite.
- 3) Compared to the central pressure minimum of a single tornado alone, a strong tornado centered within a parent mesocyclone has a larger central pressure deficit, as demonstrated in experiments A–G. On the other hand, a weak tornado in its developing stage embedded in a strong, steady-state mesocyclone, as shown in experiment H, experiences a larger central pressure deficit. It is suggested that the “observed” central pressure deficit due to the tornado alone may be overestimated.

The relative contribution of the parent mesocyclone to the low pressure at the center of a tornado is unknown. The significance of this analytical study is that one can isolate the impacts of the mesocyclone and the tornado and thus gain an understanding, in a variety of situations, of the relative contributions of each to the tornadoes' minimum pressure. Although our parametric model, complemented with cyclostrophic balance and quasi-steady-state assumptions, is quite useful for understanding the variability in the tangential velocity and deduced pressure deficit fields for the given range of input parameters, our knowledge, scrutiny, and interpretation of the effects of larger-scale vortex variability on tornado pressure minima are hypothetical, owing to the limited utility of the parametric model and also to the lack of in situ wind and pressure data from real tornadoes that would be most helpful for validating the model representation. It is recommended that a credible investigation of the model representation be involved using ultra-high-resolution numerical model output (e.g., Lewellen 2014 or Orf et al. 2014) of the wind and pressure fields in a tornado-like vortex centered within a larger-scale, background vortex.

Accurate estimates of real-life tornado wind speed maxima and pressure minima are very difficult to measure, owing to several factors. First, estimates of near-ground wind speed peaks and central pressure minima provided by Davies-Jones and Kessler (1974) are based mostly on damage and thus have a large degree of uncertainty given known complexities in estimating wind speed from damage (Doswell et al. 2009). Second, the tornadoes change intensity quite rapidly and are not necessarily steady state (Bluestein 2013). Also, they have very complex structures such as wind asymmetries, multiple vortices, vortex breakdown, turbulent boundary layers, transient phenomena, etc. Additional pressure deficits could be associated with a different vortex structure, deviations from cyclostrophic balance (e.g., Wakimoto et al. 2003), or, to a lesser extent, to the asymmetric part of the wind field (e.g., Bluestein et al. 2003). Wurman et al. (2007) showed that different tornadoes have substantially different tangential wind field structures, and both the horizontal and vertical distributions of winds differed markedly from one tornado to another. Third, the sampling frequency of deployable instrumentation within close range of an intercepted tornado (e.g., Karstens et al. 2010) was critical in determining whether true pressure deficit and maximum winds were captured. High (low) frequencies in the sampling would sufficiently (inadequately) resolve the characteristics of a tornado if the tornado's vortex

passed directly over or nearby in situ probes. It is possible that some pressure deficit measurements were erroneous as a result of instrument damping and sluggish responses (Davies-Jones 1986), because pressure gradients were very intense in tornadoes. Fourth, surface roughness can make recorded velocity and pressure data near the intercepted tornado more difficult to interpret, because surface roughness significantly affected the near-surface turbulence (Karstens et al. 2010). Fifth, it is not straightforward to surmise the vortex structure by scrutinizing the shape profiles of recorded pressure drops, because the current generation of in situ probes, in our belief, is lacking the spatiotemporal resolution for investigators to effectively disengage the exact pressure deficit contributions from vortices of different scales.

Anemometers are typically mounted in an exposed position and are therefore more susceptible to failure in tornadoes than are hardened barometers that measure the dynamic pressure change due to airflow. State-of-the-art observing systems with the capacity to measure the surface layer of intercepted tornadoes typically measure pressure (e.g., Bluestein and Golden 1993; Schroeder and Weiss 2008; Weiss and Schroeder 2008; Karstens et al. 2010) rather than wind speed, with a few exceptions (Bedard and Ramzy 1983; Wurman et al. 2012). The same is true of current instruments that take meteorological measurements at heights corresponding to the intercepted tornadoes' inertial layer [e.g., drones, radiosondes, pitot tubes on aircraft; Elston et al. (2015)]. As a result, formulating any analytical or parametric model (such as the one in this study) in terms of pressure field allows for more straightforward comparison with anticipated future observations.

*Acknowledgments.* The authors appreciate the constructive comments on an earlier version of the manuscript provided by Qin Xu, Corey Potvin, and Louis Wicker of NSSL and Alan Shapiro of University of Oklahoma. Rodger Brown, Don Burgess, Chris Karstens, and Jeff Snyder of NSSL; Howie Bluestein, Brian Fiedler, and Jerry Straka of University of Oklahoma; and Dave Lewellen of West Virginia University provided helpful discussion. The authors are grateful to Joshua Wurman of the Center for Severe Weather Research for offering us his DOW radar images illustrated in Fig. 1. The DOW radars are an NSF Lower Atmospheric Observing Facility supported by NSF-AGS-1361237. Our study is independent of this NSF grant. The authors also acknowledge Yvette Richardson of The Pennsylvania State University and the three anonymous reviewers of this manuscript, whose comments and suggestions greatly improved its scope and clarity.

## REFERENCES

- Bedard, A. J., Jr., and C. Ramzy, 1983: Surface meteorological observations in severe thunderstorms. Part I: Design details of TOTO. *J. Climate Appl. Meteor.*, **22**, 911–918, doi:10.1175/1520-0450(1983)022<0911:SMOIST>2.0.CO;2.
- Blair, S. F., D. R. Deroche, and A. E. Pietrycha, 2008: In situ observations of the 21 April 2007 Tulia, Texas tornado. *Electron. J. Severe Local Storms Meteor.*, **3** (3). [Available online at <http://www.ejssm.org/ojs/index.php/ejssm/article/view/39>.]
- Bluestein, H. B., 1983: Surface meteorological observations in severe thunderstorms. Part II: Field experiments with TOTO. *J. Climate Appl. Meteor.*, **22**, 919–930, doi:10.1175/1520-0450(1983)022<0919:SMOIST>2.0.CO;2.
- , 2013: *Severe Convective Storms and Tornadoes: Observations and Dynamics*. Springer-Verlag, 456 pp.
- , and J. H. Golden, 1993: A review of tornado observations. *The Tornado: Its Structure, Dynamics, Prediction, and Hazards, Geophys. Monogr.*, Vol. 79, Amer. Geophys. Union, 319–352.
- , W.-C. Lee, M. Bell, C. C. Weiss, and A. L. Pazmany, 2003: Mobile Doppler radar observations of a tornado in a supercell near Bassett, Nebraska, on 5 June 1999. Part II: Tornado-vortex structure. *Mon. Wea. Rev.*, **131**, 2968–2984, doi:10.1175/1520-0493(2003)131<2968:MDROOA>2.0.CO;2.
- , J. B. Houser, M. M. French, J. C. Snyder, G. D. Emmitt, I. PopStefanija, C. Baldi, and R. T. Bluth, 2014: Observation of the boundary layer near tornadoes and in supercells using a mobile, collocated, pulsed Doppler lidar and radar. *J. Atmos. Oceanic Technol.*, **31**, 302–325, doi:10.1175/JTECH-D-13-00112.1.
- Brooks, E. M., 1949: The tornado cyclone. *Weatherwise*, **2** (2), 32–33, doi:10.1080/00431672.1949.9930047.
- Burgers, J. M., 1948: A mathematical model illustrating the theory of turbulence. *Adv. Appl. Mech.*, **1**, 197–199.
- Davies-Jones, R. P., 1986: Tornado dynamics. *Thunderstorm Morphology and Dynamics*, 2nd ed. E. Kessler, Ed., University of Oklahoma Press, 197–236.
- , 2008: Can a descending rain curtain in a supercell instigate tornadogenesis barotropically? *J. Atmos. Sci.*, **65**, 2469–2497, doi:10.1175/2007JAS2516.1.
- , and E. Kessler, 1974: Tornadoes. *Weather and Climate Modification*, W. N. Hess, Ed., John Wiley and Sons, 552–595.
- Doswell, C. A., III, H. E. Brooks, and N. Dotzek, 2009: On the implementation of the enhanced Fujita scale in the USA. *Atmos. Res.*, **93**, 554–563, doi:10.1016/j.atmosres.2008.11.003.
- Elston, J., B. Argrow, M. Stachura, D. Weibel, D. Lawrence, and D. Pope, 2015: Overview of small fixed-wing unmanned aircraft for meteorological sampling. *J. Atmos. Oceanic Technol.*, **32**, 97–115, doi:10.1175/JTECH-D-13-00236.1.
- Hoecker, W. H., Jr., 1961: Three-dimensional pressure pattern of the Dallas tornado and some resultant implications. *Mon. Wea. Rev.*, **89**, 533–542, doi:10.1175/1520-0493(1961)089<0533:TPPOTD>2.0.CO;2.
- Inoue, H. Y., and Coauthors, 2011: Finescale Doppler radar observations of a tornado and low-level mesocyclones within a winter storm in the Japan Sea coastal region. *Mon. Wea. Rev.*, **139**, 351–369, doi:10.1175/2010MWR3247.1.
- Karstens, C. D., T. M. Samaras, B. D. Lee, W. A. Gallus Jr., and C. A. Finley, 2010: Near-ground pressure and wind measurements in tornadoes. *Mon. Wea. Rev.*, **138**, 2570–2588, doi:10.1175/2010MWR3201.1.
- Kato, R., and Coauthors, 2015: Analysis of the horizontal two-dimensional near-surface structure of a winter tornadic vortex

- using high-resolution in situ wind and pressure measurements. *J. Geophys. Res. Atmos.*, **120**, 5879–5894, doi:10.1002/2014JD022878.
- Knaff, J. A., C. R. Sampson, P. J. Fitzpatrick, Y. Jin, and C. M. Hill, 2011: Simple diagnosis of tropical cyclone structure via pressure gradients. *Wea. Forecasting*, **26**, 1020–1031, doi:10.1175/WAF-D-11-00013.1.
- Kosiba, K. A., P. Robinson, P. W. Chan, and J. Wurman, 2014: Wind field of a nonmesocyclone anticyclonic tornado crossing the Hong Kong International Airport. *Adv. Meteor.*, **2014**, 597378, doi:10.1155/2014/597378.
- Lee, J. J., T. M. Samaras, and C. R. Young, 2004: Pressure measurements at the ground in an F-4 tornado. *22nd Conf. on Severe Local Storms*, Hyannis, MA, Amer. Meteor. Soc., 15.3. [Available online at [https://ams.confex.com/ams/11aram22s/techprogram/paper\\_81700.htm](https://ams.confex.com/ams/11aram22s/techprogram/paper_81700.htm).]
- Lee, W.-C., and J. Wurman, 2005: Diagnosed three-dimensional axisymmetric structure of the Mulhall tornado on 3 May 1999. *J. Atmos. Sci.*, **62**, 2373–2393, doi:10.1175/JAS3489.1.
- Leverson, V. H., P. C. Sinclair, and J. H. Golden, 1977: Waterspout wind, temperature, and pressure structure deduced from aircraft measurements. *Mon. Wea. Rev.*, **105**, 725–733, doi:10.1175/1520-0493(1977)105<0725:WWTAPS>2.0.CO;2.
- Lewellen, D. C., 2014: Local roughness effects on tornado dynamics. *27th Conf. on Severe Local Storms*, Madison, WI, Amer. Meteor. Soc., 15A.1. [Available online at <https://ams.confex.com/ams/27SLS/webprogram/Paper254357.html>.]
- , and W. S. Lewellen, 2007: Near-surface intensification of tornado vortices. *J. Atmos. Sci.*, **64**, 2176–2194, doi:10.1175/JAS3965.1.
- , —, and J. Xia, 2000: The influence of a local swirl ratio on tornado intensification near the surface. *J. Atmos. Sci.*, **57**, 527–544, doi:10.1175/1520-0469(2000)057<0527:TIOALS>2.0.CO;2.
- Markowski, P. M., J. M. Straka, and E. N. Rasmussen, 2002: Direct surface thermodynamic observations within the rear-flank downdrafts of nontornadic and tornadic supercells. *Mon. Wea. Rev.*, **130**, 1692–1721, doi:10.1175/1520-0493(2002)130<1692:DSTOWT>2.0.CO;2.
- Marquis, J., Y. Richardson, J. Wurman, and P. Markowski, 2008: Single- and dual-Doppler analysis of a tornadic vortex and surrounding storm-scale flow in the Crowell, Texas, supercell of 30 April 2000. *Mon. Wea. Rev.*, **136**, 5017–5043, doi:10.1175/2008MWR2442.1.
- McDonald, J. R., G. S. Forbes, and T. P. Marshall, 2004: The enhanced Fujita (EF) scale. Preprints, *22nd Conf. on Severe Local Storms*, Hyannis, MA, Amer. Meteor. Soc., 3B.2. [Available online at <http://ams.confex.com/ams/pdfpapers/81090.pdf>.]
- Orf, L., R. B. Wilhelmson, L. J. Wicker, B. D. Lee, and C. A. Finley, 2014: Genesis and maintenance of a long-track EF5 tornado embedded within a simulated supercell. *27th Conf. on Severe Local Storms*, Madison, WI, Amer. Meteor. Soc., 3B.3. [Available online at <https://ams.confex.com/ams/27SLS/webprogram/Paper255451.html>.]
- Rankine, W. J. M., 1882: *A Manual of Applied Physics*. 10th ed. Charles Griff and Co., 663 pp.
- Rasmussen, E. N., J. M. Straka, R. Davies-Jones, C. A. Doswell III, F. H. Carr, M. D. Eilts, and D. R. MacGorman, 1994: Verification of the Origins of Rotation in Tornadoes Experiment: VORTEX. *Bull. Amer. Meteor. Soc.*, **75**, 995–1006, doi:10.1175/1520-0477(1994)075<0995:VOTOOR>2.0.CO;2.
- Rennó, N. O., and H. B. Bluestein, 2001: A simple theory for waterspouts. *J. Atmos. Sci.*, **58**, 927–932, doi:10.1175/1520-0469(2001)058<0927:ASTFW>2.0.CO;2.
- , M. L. Burkett, and M. P. Larkin, 1998: A simple thermodynamical theory for dust devils. *J. Atmos. Sci.*, **55**, 3244–3252, doi:10.1175/1520-0469(1998)055<3244:ASTTFD>2.0.CO;2.
- Rott, N., 1958: On the viscous vortex of a line vortex. *Z. Angew. Math. Phys.*, **9**, 543–553, doi:10.1007/BF02424773.
- Samaras, T. M., and J. J. Lee, 2004: Pressure measurements within a large tornado. *Eighth Symp. on Integrated Observing and Assimilation for Atmosphere, Oceans, and Land Surface*, Seattle, WA, Amer. Meteor. Soc., 4.9. [Available online at [https://ams.confex.com/ams/84Annual/techprogram/paper\\_74267.htm](https://ams.confex.com/ams/84Annual/techprogram/paper_74267.htm).]
- Schroeder, J. L., and C. C. Weiss, 2008: Integrating research and education through measurement and analysis. *Bull. Amer. Meteor. Soc.*, **89**, 793–798, doi:10.1175/2008BAMS2287.1.
- Sinclair, P. C., 1973: The lower structure of dust devils. *J. Atmos. Sci.*, **30**, 1599–1619, doi:10.1175/1520-0469(1973)030<1599:TLSODD>2.0.CO;2.
- Snow, J. T., 1982: A review of recent advances in tornado vortex dynamics. *Rev. Geophys. Space Phys.*, **20**, 953–964, doi:10.1029/RG020i004p00953.
- Tanamachi, R. L., H. B. Bluestein, M. Xue, W.-C. Lee, K. A. Orzel, S. J. Frasier, and R. M. Wakimoto, 2013: Near-surface vortex structure in a tornado and in a sub-tornado-strength, convective-storm vortex, observed by a mobile, W-band radar during VORTEX2. *Mon. Wea. Rev.*, **141**, 3661–3690, doi:10.1175/MWR-D-12-00331.1.
- Wakimoto, R. M., and J. W. Wilson, 1989: Non-supercell tornadoes. *Mon. Wea. Rev.*, **117**, 1113–1140, doi:10.1175/1520-0493(1989)117<1113:NST>2.0.CO;2.
- , H. V. Murphey, D. C. Dowell, and H. B. Bluestein, 2003: The Kellerville tornado during VORTEX: Damage survey and Doppler radar analyses. *Mon. Wea. Rev.*, **131**, 2197–2221, doi:10.1175/1520-0493(2003)131<2197:TKTDVD>2.0.CO;2.
- , N. T. Atkins, K. M. Butler, H. B. Bluestein, K. Thiem, J. Snyder, and J. Houser, 2015: Photogrammetric analysis of the 2013 El Reno tornado combined with mobile X-band polarimetric radar data. *Mon. Wea. Rev.*, **143**, 2657–2683, doi:10.1175/MWR-D-15-0034.1.
- Weiss, C. C., and J. L. Schroeder, 2008: StickNet—A new portable, rapidly deployable, surface observing system. *25th Int. Conf. on Interactive Information Processing Systems for Meteorology, Oceanography, and Hydrology*, New Orleans, LA, Amer. Meteor. Soc., P4A.1. [Available online at [https://ams.confex.com/ams/88Annual/techprogram/paper\\_134047.htm](https://ams.confex.com/ams/88Annual/techprogram/paper_134047.htm).]
- Wicker, L. J., and R. B. Wilhelmson, 1993: Numerical simulation of tornadogenesis within a supercell thunderstorm. *The Tornado: Its Structure, Dynamics, Prediction, and Hazards*, Geophys. Monogr., Vol. 79, Amer. Geophys. Union, 75–88.
- Winn, W. P., S. J. Hunyady, and G. D. Aulich, 1999: Pressure at the ground in a large tornado. *J. Geophys. Res.*, **104**, 22 067–22 082, doi:10.1029/1999JD900387.
- Wood, V. T., and R. A. Brown, 2011: Simulated tornadic vortex signatures of tornado-like vortices having one- and two-celled structures. *J. Appl. Meteor. Climatol.*, **50**, 2338–2342, doi:10.1175/JAMC-D-11-0118.1.
- , and L. W. White, 2013: A parametric wind–pressure relationship for Rankine versus non-Rankine cyclostrophic vortices. *J. Atmos. Oceanic Technol.*, **30**, 2850–2867, doi:10.1175/JTECH-D-13-00041.1.
- , —, H. E. Willoughby, and D. P. Jorgensen, 2013: A new parametric tropical cyclone tangential wind profile model. *Mon. Wea. Rev.*, **141**, 1884–1909, doi:10.1175/MWR-D-12-00115.1.
- WSEC, 2006: A recommendation for an enhanced Fujita scale (EF-scale). Wind Science and Engineering Center Tech.

- Rep., Texas Tech University, 15 pp + 3 appendixes. [Available online at <http://www.depts.ttu.edu/nwi/Pubs/FScale/EFScale.pdf>.]
- Wurman, J., 2002: The multiple-vortex structure of a tornado. *Wea. Forecasting*, **17**, 473–505, doi:10.1175/1520-0434(2002)017<0473:TMVSOA>2.0.CO;2.
- , and S. Gill, 2000: Finescale radar observations of the Dimmitt, Texas (2 June 1995), tornado. *Mon. Wea. Rev.*, **128**, 2135–2164, doi:10.1175/1520-0493(2000)128<2135:FROOTD>2.0.CO;2.
- , and T. Samaras, 2004: Comparison of in-situ pressure and DOW Doppler winds in a tornado and RHI vertical slices through 4 tornadoes during 1996–2004. *22nd Conf. on Severe Local Storms*, Hyannis, MA, Amer. Meteor. Soc., 15.4. [Available online at [https://ams.confex.com/ams/11aram22sls/techprogram/paper\\_82352.htm](https://ams.confex.com/ams/11aram22sls/techprogram/paper_82352.htm).]
- , and C. R. Alexander, 2005: The 30 May 1998 Spencer, South Dakota, storm. Part II: Comparison of observed damage and radar-derived winds in the tornadoes. *Mon. Wea. Rev.*, **133**, 97–119, doi:10.1175/MWR-2856.1.
- , and K. Kosiba, 2013: Finescale radar observations of tornado and mesocyclone structures. *Wea. Forecasting*, **28**, 1157–1174, doi:10.1175/WAF-D-12-00127.1.
- , J. Straka, E. Rasmussen, M. Randall, and A. Zahrai, 1997: Design and deployment of a portable, pencil-beam, pulsed, 3-cm Doppler radar. *J. Atmos. Oceanic Technol.*, **14**, 1502–1512, doi:10.1175/1520-0426(1997)014<1502:DADOAP>2.0.CO;2.
- , C. R. Alexander, P. Robinson, and Y. Richardson, 2007: Low-level winds in tornadoes and potential catastrophic tornado impacts in urban areas. *Bull. Amer. Meteor. Soc.*, **88**, 31–46, doi:10.1175/BAMS-88-1-31.
- , D. Dowell, Y. Richardson, P. Markowski, E. Rasmussen, D. Burgess, L. Wicker, and H. Bluestein, 2012: The Second Verification of the Origins of Rotation in Tornadoes Experiment: VORTEX2. *Bull. Amer. Meteor. Soc.*, **93**, 1147–1170, doi:10.1175/BAMS-D-11-00010.1.
- , K. Kosiba, P. Robinson, and T. Marshall, 2014: The role of multiple-vortex tornado structure in causing storm researcher fatalities. *Bull. Amer. Meteor. Soc.*, **95**, 31–45, doi:10.1175/BAMS-D-13-00221.1.